NANO · MICRO small
www.small-journal.com

Dramatic Responsivity Enhancement Through Concentrated H_2SO_4 Treatment on PEDOT:PSS/TiO_2 Heterojunction Fibrous Photodetectors

Xiaolei Deng, Ziliang Li, Hui Liu, Yijian Zhao, Lingxia Zheng, Xiaowei Shi, Liang Wang, Xiaosheng Fang,* and Huajun Zheng**

In order to satisfy the growing requirements of wearable electronic devices, 1D fiber-shaped devices with outstanding sensitivity, flexibility, and stability are urgently needed. In this study, a novel inorganic-organic heterojunction fibrous photodetector (FPD) based on poly(3,4-ethylenedioxythiophene):polystyrene sulfonate (PEDOT:PSS) and highly ordered TiO_2 nanotube array is fabricated, which endows a high responsivity, large external quantum efficiency, and fast response speed at 3 V bias. To further ameliorate its performance in the self-powered mode, a facile acid treatment is adopted and the assembled H-PEDOT:PSS/TiO_2 FPD demonstrates outstanding self-powered properties with ≈3000% responsivity enhancement (161 mA W^{-1} at 0 V under 365 nm irradiation, photocurrent enhancement of ≈50 times) compared with the untreated device. It is found that the concentrated H_2SO_4 post-treatment helps decrease the tube wall thickness of TiO_2 and partially removes the insulated PSS component in PEDOT:PSS, leading to enhanced conductivity and facilitated charge transportation, and thereby superb responsivity/photocurrent enhancement of self-powered H-PEDOT:PSS/TiO_2 FPD. This low-cost and high-performance self-powered FPD shows high potential for applications in wearable electronic devices.

1. Introduction

Wearable electronic devices have important practical significance in the emerging innovative applications such as health monitoring,[1] atrial fibrillation detection,[2] electromagnetic shielding,[3] physiological markers,[4] wearable transistors,[5] photovoltaics,[6] photodetectors (PDs),[7] etc. In particular, fiber-shaped flexible devices are booming as a nominated and multifunctional apparatus due to their unique geometry, portability, knittability, and mechanical strength.[8–11] The fibrous devices could be woven into a large variety of fabric-based functional devices.[12] However, compared to planar counterparts, the fibrous devices generally display distinct aspect-ratio and mini-type configuration, leading to intricate stress–strain situation at the reduplicative bending and stretching deformation. Therefore, the first primary issue is to guarantee compact and robust contact between the fibrous substrate and photoactive material to assure stable and solid performance under deformation.[13–15] In this regard, metal fibers that can serve as both electrode and precursor are representative substrate candidates for the fibrous devices, benefitting from their advantages such as good flexibility, high conductivity, and low cost.

PDs, which transform light irradiation to electrical signal, have been extensive used in various fields of military and national economics, such as flame detection, radioactive measurement, infrared thermal imaging, memristor, and so forth.[16,17] Recently, fibrous PDs (FPDs) have attracted great attention because of their significant application prospect in wearable devices which require flexibility, light-weight, and softness. Besides the common "5S" key parameters,[18,19] extra features need to be considered for FPDs: 1) high level of flexibility and toughness which allows it to be operated steadily in a rigorous circumstance; 2) self-powered property without an external power system, which endows merits of zero-maintenance and energy-saving. Specifically, the self-powered PDs can be realized through the construction of p–n junctions, Schottky junctions, and heterojunctions[20–22] as the built-in electric field enables efficient separation of photo-excited electron–hole pairs due to the photovoltaic effect. To date, several attempts have been made to manufacture self-powered flexible FPDs. For instance, Zeng et. al.[23] have presented a self-powered wearable omnidirectional UV FPD with a responsivity of 9.96 mA W^{-1} and an on/off ratio of 2 at zero bias. Li et. al.[24] have reported a

X. L. Deng, Y. J. Zhao, Dr. L. X. Zheng, Dr. X. W. Shi, Prof. H. J. Zheng
Department of Applied Chemistry
Zhejiang University of Technology
Hangzhou 310032, P. R. China
E-mail: lxzheng@zjut.edu.cn; zhenghj@zjut.edu.cn
Dr. Z. L. Li, Dr. H. Liu, Prof. X. S. Fang
Department of Materials Science
Fudan University
Shanghai 200433, P. R. China
E-mail: xshfang@fudan.edu.cn
Dr. L. X. Zheng, Dr. X. W. Shi, Prof. L. Wang, Prof. H. J. Zheng
State Key Laboratory Breeding Base of Green Chemistry Synthesis Technology
Zhejiang University of Technology
Hangzhou 310032, P. R. China
The ORCID identification number(s) for the author(s) of this article can be found under https://doi.org/10.1002/smll.202101674.

DOI: 10.1002/smll.202101674

novel self-powered broadband FPD with an ultrahigh detectivity (10^{13} Jones), which consists of double-twisted perovskite-TiO_2-carbon fiber and CuO-Cu_2O-Cu wire. A novel self-powered Au/TiO_2/P3HT FPD with a responsivity enhancement of nearly 700% compared with the TiO_2/P3HT counterpart device has been reported.[25] Given the crooked and tiny irradiated area of photoactive materials, it is still a big challenge to yield considerable photoresponse (responsivity, photocurrent, sensitivity) on FPDs. Moreover, it is also imperative to explore novel and effective heterojunction via a facile and economic route and thereby enabling high-performance self-powered FPDs.

Inorganic–organic hybrid heterojunctions afford a promising way to realize high-performance FPDs with high flexibility and even self-powered characteristics.[26,27] Highly ordered 1D TiO_2 nanotubes (NTs) have been proved to be one of the most promising material candidates due to the appealing light-trapping characteristics and the facilitated charge transport pathway as well as the common merits of high carrier mobility, high UV light absorption, and advantageous band edge positions.[28–30] Recently, p-type organic polymers have been extensively utilized for the construction of wearable devices owing to their unique advantages, such as low-cost, compatibility, functionality, and flexibility. Particularly, as a highly π-conjugated organic polymer, PEDOT:PSS (poly(3,4-ethylene dioxythiophene):polystyrene sulfonate) which compose of hydrophobic conducting PEDOT-rich grains and hydrophilic insulating PSS-rich shells, has been widely used as a hole transporting layer in photovoltaic devices due to its suitable work function, high optical transmittance (above 90%) and good mechanical flexibility.[31–34] Nevertheless, further applications of this organic semiconductor for the construction of heterojunctions are greatly restrained due to its poor optoelectronic performance that is related to low conductivity.[35,36] Recently, various facile ways have been reported to modify the conductivity of PEDOT:PSS such as organic solvents (dimethylsulfoxide, methanol), surfactants, salts, and acids.[36–38] The primary reason for the conductivity enhancement is owing to the intentional removal of insulating PSS component to a certain extent and thus alleviating the structural order of conducting PEDOT domain. Impressively, among various kinds of acids (e.g., HNO_3, HCOOH, HCl), the H_2SO_4-treated PEDOT:PSS is reported to perform best in conductivity,[39] which is even comparable to the conductivity of ITO when properly treating the PEDOT:PSS solution precursor (1.0–1.3 wt% in water).[40] Notwithstanding these achievements, the reports on modified PEDOT: PSS-based optoelectronic devices are scarce, let alone the 1D flexible/wearable devices.

In this scenario, we have prepared 1D anodic TiO_2 NTs that are in situ grown on the surface of Ti microwire to guarantee compact and robust contact between the oxide and Ti electrode. The uniform loading of PEDOT:PSS is followed a vacuum impregnation method to prepare PEDOT:PSS/TiO_2 heterojunction hybrid. The rational engineered p–n interface enables high-performance photodetecting capability (responsivity of 348.5 A W^{-1}, external quantum efficiency of 1.2×10^5% at 3 V) with outstanding flexibility and fast response speed. Besides, it also demonstrates self-powered property with a response speed of less than 1 s (0.62 s/0.54 s), and a responsivity of 5.1 mA W^{-1} at zero bias under 365 nm UV illumination. Interestingly, a simple acid treatment is applied to dramatically enhance the self-powered photoresponse and responsivity enhancement of ≈3000% has been realized. The high responsivity (161 mA W^{-1}) at 0 V bias is comparable to the recently reported best values on FPDs in literature (Table S1, Supporting Information).

2. Result and Discussion

The X-ray diffraction (XRD) patterns of the TiO_2 NTs, H-TiO_2 NTs, PEDOT:PSS/TiO_2 hybrid, and H-PEDOT:PSS/TiO_2 hybrid are shown in **Figure 1**a. Five characteristic peaks located at $2\theta =$ 25.2, 37.8, 48.0, 53.9, 55.0 can be assigned to (101), (004), (200), (105), (211) planes of anatase TiO_2 (JCPDS 21-1272), respectively, while other sharp diffraction peaks are assigned to metallic Ti fibers (JCPDS 44-1294). On account of the low content of PEDOT:PSS that is far below the detection limit of the equipment, no obvious signals for PEDOT:PSS can be detected. And no detectable change can be observed upon PEDOT:PSS impregnation for PEDOT:PSS/TiO_2 hybrid. Notably, the (101) peak intensity assigning to TiO_2 is obviously decreased for the two acid-treated samples H-TiO_2 and H-PEDOT:PSS/TiO_2, which suggests the low crystallinity of modified TiO_2 domain.[41,42] Raman spectroscopy is performed on the samples to further verify the existence of PEDOT:PSS in the hybrids. In the range of 50–1000 cm^{-1} (Figure S1, Supporting Information), all the samples exhibit a similar profile that can be assigned to anatase TiO_2, indicating the exceptional good stability of TiO_2 backbone.[43] In addition, the conformational change of PEDOT:PSS chains can be observed in the range of 1300–1600 cm^{-1} without any trace for TiO_2 (Figure 1b). The dominant peak at 1435 cm^{-1} matches the symmetric stretching modes of C_α=C_β while three small peaks at 1503, 1537, and 1558 cm^{-1} are assigned to asymmetric stretching modes of C_α=C_β of benzoid structure. The subordinate peak centered at 1362 cm^{-1} originates from the symmetric stretching modes of C_α−C_β of quinoid structure for PEDOT.[31,44,45] For H-PEDOT:PSS/TiO_2, the intensity of all the characteristic peaks assigning to PEDOT increases, suggesting the exposure of PEDOT domain after acid treatment. Impressively, the peak assigning to symmetric C_α=C_β stretching redshifts from 1435 to 1425 cm^{-1}, suggesting the transformation from benzoid to quinoid structure, so that the quinoid character becomes dominant in H-PEDOT:PSS/TiO_2 (Figure 1c).[31,44–46] In contrast, the peak assigning to asymmetric C_α=C_β stretching blueshifts from 1503 to 1508 cm^{-1}, which indicates the existence of an intermediate electronic structure of the neutral polymer besides the usual scheme of benzoid–quinoid structure.[45,47]

Figure 2 reveals the microscopic morphological characteristics of the H-PEDOT:PSS/TiO_2 hybrid, PEDOT:PSS/TiO_2 hybrid, and TiO_2NTs on Ti micro-fibers. A conventional two-step anodization method is used to grow 1D highly-ordered TiO_2 NTs arrays on Ti metal fibers. The TiO_2NTs sample displays well-aligned tubular arrays with the length of ≈4 µm, and the diameter of the outer NTs ranges from 100 to 150 nm (Figure 2a–c). The hollow NTs with neat top-surface provide easy access for the loading of organic polymers. The PEDOT:PSS/TiO_2 hybrid was prepared using a vacuum impregnation method, and the conductive PEDOT:PSS polymers are overlaid on both the outer-tube walls and tube top-surface (Figure 2d–f). Owing to

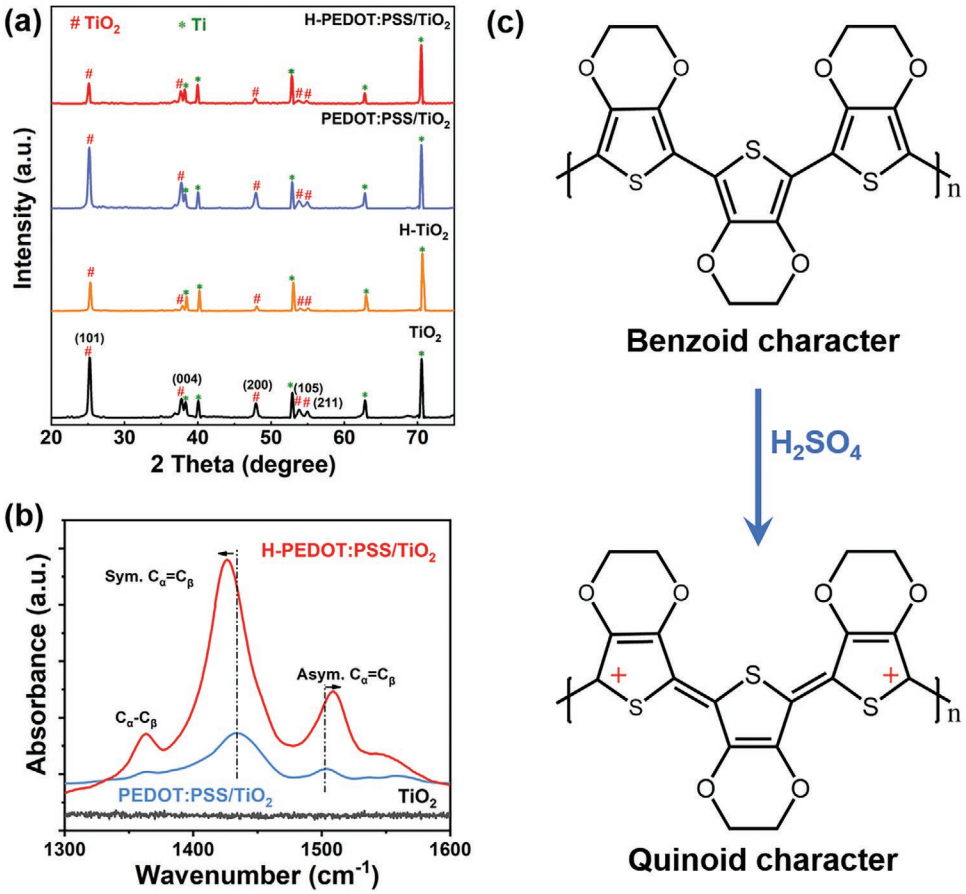

Figure 1. a) XRD patterns and b) Raman spectra of different samples. c) Molecular structural changes of PEDOT after acid treatment.

the strong capillary force, the PEDOT:PSS ethyl alcohol solution can easily penetrate the inter-tubular gaps with full contact with TiO_2 NTs. As a result, a PEDOT:PSS thin film is formed at the outer tube walls accompanied with small nanoparticles on the tube mouths. The morphology of retained highly-ordered nanotubular array is beneficial to the well-defined carrier transport pathway. The X-ray energy dispersive spectroscopy (SEM-EDS) mapping images (lateral view in Figure S2a, Supporting Information and whole fiber in Figure S3, Supporting Information) clearly demonstrate the homogeneously distributed Ti, O, and S elements. It is noteworthy that the intimate and full contact between the conducting polymers and TiO_2 NTs is beneficial for the effective construction of p–n heterojunction, which facilitates the effective separation of photogenerated electron-hole pairs and even facilitates the generation of self-powered property.[23] Moreover, in order to optimize the conductivity of PEDOT:PSS, facile acid treatment is employed to intentionally remove the insulating PSS and the obtained sample is termed as H-PEDOT:PSS/TiO_2 hybrid. Figure S2b, Supporting Information, reveals that elements Ti, O, and S are existed and evenly distributed in H-PEDOT:PSS/TiO_2, validating the intimate and uniform contact between PEDOT:PSS and TiO_2 NTs. The SEM images in Figure 2g–i reveal that the granular PEDOT:PSS polymers evolve into the nanofibers following the charge-separated transition mechanism.[40] Interestingly, it can be observed that the tube walls of TiO_2 for H-PEDOT:PSS/TiO_2 hybrid become thinner (Figure 2e,h), which is also verified by the SEM images of H-TiO_2 sample (Figure S4, Supporting Information). As reported,[48] the degree of crystallinity of TiO_2 was found to increase with increasing NT wall thickness. Herein, the decreased crystallinity of H-TiO_2 and H-PEDOT:PSS/TiO_2 (XRD patterns, Figure 1a) is probably originated from the decreased tube wall thickness of TiO_2. Accordingly, the thickness of PEDOT:PSS layer residing on the tube walls is also reduced, which is beneficial to the intimate contact between organic polymer and TiO_2 NTs.

Transmission electron microscopy (TEM) images reveal the detailed morphological change of PEDOT:PSS/TiO_2 (**Figure 3**a–d) and H-PEDOT:PSS/TiO_2 (Figure 3e–h). The PEDOT:PSS layer is amorphous and can be found along the TiO_2 tube walls. By comparison, the thickness of the polymer film is greatly decreased from 40 nm (Figure 3b) to 5 nm (Figure 3f) after acid treatment. The distinct lattice fringes (spacing of 0.348 nm in Figure 3c and 0.346 nm in Figure 3g) match the (101) plane of anatase TiO_2, consistent with XRD results. The elemental mapping images in Figure 3d,h further verify the existence of elements Ti, O, and S in the two hybrids, consistent with the SEM results.

The assembly scheme of fibrous PD device is revealed in Scheme S1, Supporting Information. The Carbon NT (CNT) yarn was served as the outer electrode by twisting tightly around the photoactive materials on Ti metal. The other end of

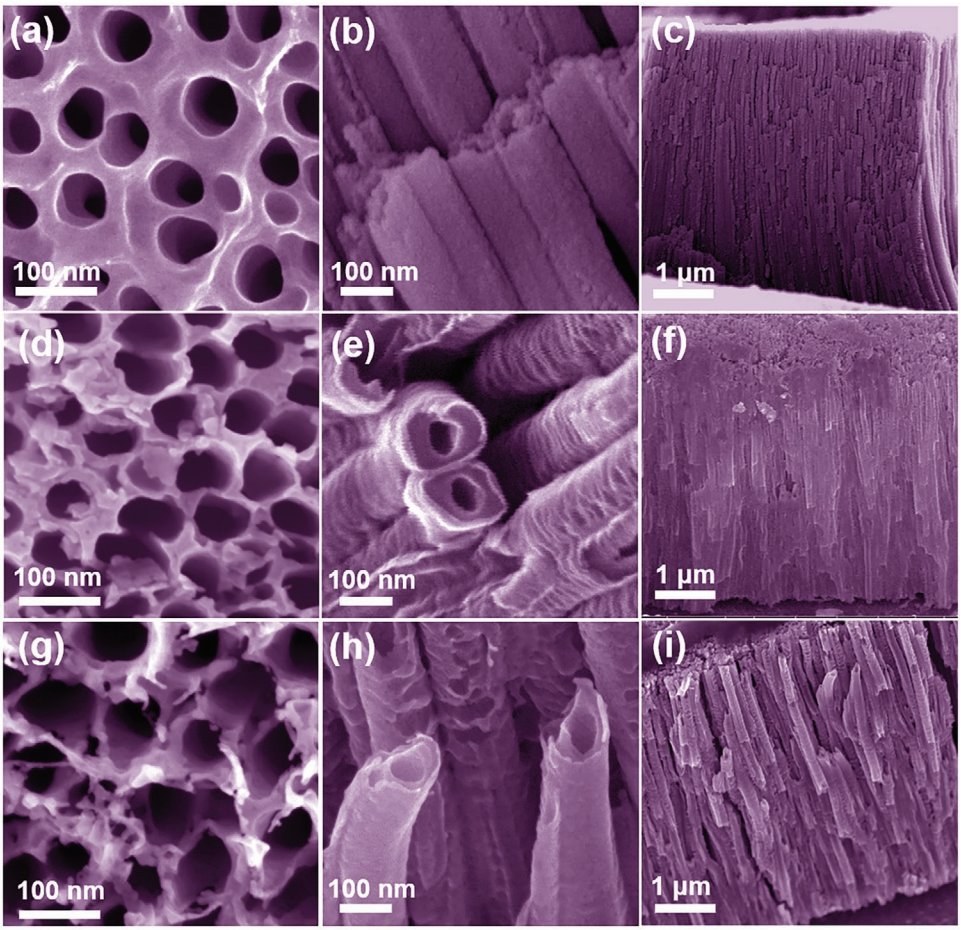

Figure 2. a–c) SEM images of TiO_2 NTs, d–f) PEDOT:PSS/TiO_2 hybrid, and g–i) H-PEDOT:PSS/TiO_2 hybrid.

Ti fiber was polished to serve as the inner electrode. The photoelectrical performance of the PEDOT:PSS/TiO_2 FPD has been characterized by a two-probe method under ambient conditions and monochromatic illumination, as shown in **Figure 4**. Noteworthy that the intimate contact between CNT yarn electrode and photoactive material (Figure S5, Supporting Information) without gaps is highly desirable for good charge collection efficiency, which contributes largely to the overall superior stable performance under deformation. Several important parameters such as spectral responsivity (R_λ), external quantum efficiency (EQE) and detectivity (D^*) to evaluate the performance are defined according to the following formulae:[18,20,49,50]

$$R_\lambda = \frac{I_p - I_d}{\mathrm{PA}} \tag{1}$$

$$\mathrm{EQE} = \frac{hc}{e\lambda} R_\lambda \tag{2}$$

$$D^* = \frac{R_\lambda}{\left(2eI_d/A\right)^{1/2}} \tag{3}$$

where I_p, I_d, P, A, and λ are the photocurrent, dark current, light power intensity, effective illumination area, and wavelength of the radiation light, respectively. The h, c, and e refer to the Planck constant, light speed, and electronic charge, respectively.

A maximum spectral responsivity of 348.5 A W^{-1} and EQE of 1.2×10^5% (Figure 4a) are achieved at 3 V bias under 365 nm UV illumination, indicating excellent photo-responsivity and high gain of the PEDOT:PSS/TiO_2 hybrid FPDs. The UV–visible rejection ratio ($R_{365\ \mathrm{nm}}/R_{400\ \mathrm{nm}}$) is calculated to be ≈453, implying high photoselectivity. The maximum D^* is calculated to be 7×10^{12} Jones (Figure S6, Supporting Information), reflecting the outstanding sensitivity, which is within an order of magnitude of the D^* for commercial Si and InGaAs PDs and exceeds the D^* for Ge PDs.[20,51] Compared these values with an earlier work on planar TiO_2 nanorod/PEDOT:PSS UV PD (EQE ≈ 1.2×10^4%, R ≈ 34.43 A W^{-1}, D^* ≈ 1.6×10^{11} Jones),[33] our 1D PEDOT:PSS/TiO_2 FPD device endows an order of magnitude higher photodetection performance (**Table 1**), demonstrating a high-performance solar-blind UV PD. The current-time (I–t) curves of PEDOT:PSS/TiO_2 device at 3 V bias with good stability is presented in Figure 4b. The photocurrent reaches as high as ≈1400 μA, almost 170 times higher than that of pure TiO_2 FPD (≈8 μA, Figure S7, Supporting Information). The on–off ratio is calculated to be 140, which is 70 times higher than that of the pure TiO_2. Meanwhile, the response speed is also increased dramatically with rise/fall time of 2.3/2.2 s (Figure S8, Supporting Information), while the pure TiO_2 device demonstrates sluggish response speed (rise/fall time of 16.5 s/22.6 s). These values verify the high performance of PEDOT:PSS/TiO_2 FPD

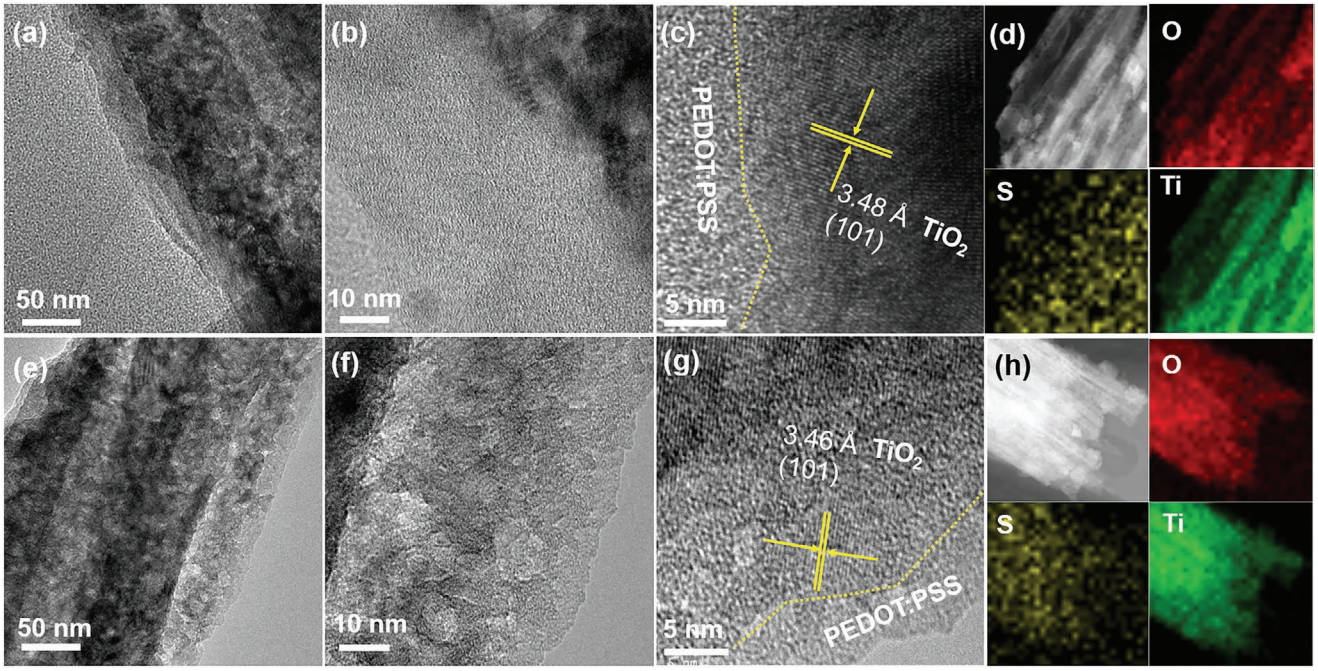

Figure 3. TEM images of a–c) PEDOT:PSS/TiO_2 and e–g) H-PEDOT:PSS/TiO_2 hybrid. EDS mapping showing the elemental distribution of Ti, O, and S of d) PEDOT:PSS/TiO_2 and h) H-PEDOT:PSS/TiO_2 hybrid, respectively.

with high responsivity, high selectivity, fast response speed, and good photosensitivity, suggesting the enormous potential application in future flexible/wearable photodetecting devices. Figure 4c shows the current–voltage (I–V) curves of pure TiO_2 and PEDOT:PSS/TiO_2 devices under dark and 365 nm light irradiation. The dark current curve of PEDOT:PSS/TiO_2 FPD has a rectification ratio of 420 at ±3 V, representing a typical photodiode characteristic. In contrast, the symmetric dark-current curve of pure TiO_2 FPD and the linear curve of pure PEDOT:PSS device (Figure S9, Supporting Information) signify the ohmic contact between CNT electrode and photoactive material. Thus, it is reasonable to conclude that the rectifying characteristics of the hybrid device are originated from the formation of heterojunction between n-TiO_2 and p-PEDOT:PSS, which is promising for the self-powered property. Furthermore, flexibility and stability under deformation are two crucial parameters to evaluate real-life wearable devices. The PEDOT:PSS/TiO_2 PFD exhibits a stable and fast UV response under 365 nm irradiation at 3 V bias when bending at different angles (i.e., 0-, 30-, 50-, 70-, 90°) (Figure 4d) and curving at 90° for 500 cycles (Figure 4e). The reason can be attributed to the good adhesion of TiO_2 in situ grown on the surface of Ti microwire and the highly flexible organic component (PEDOT:PSS).

The self-powered photoelectric performance of PEDOT:PSS/TiO_2 FPD at zero bias is shown in **Figure 5**. The responsivity at zero bias increases with the decrease of wavelength in the range of 280–600 nm. The maximum responsivity is 11.2 mA W^{-1} under 200 nm illumination, and the weak/small peak at 365 nm illumination is calculated to be 5.1 mA W^{-1} (Figure 5a). The UV–visible rejection ratio (R_{365}/R_{400}) is calculated to be ≈2 at zero bias, which is much lower than the value at 3 V bias (≈453). This significant variation is interpreted by a great increase in responsivity/photocurrent at 3 V under 365 nm UV illumination based on Equation (1). Upon UV light illumination, when applying a forward bias (+3 V), the width of the depletion layer becomes narrow and the majority carriers can transport through the depletion layer driven by the applied bias and thus generating large photocurrent (≈1.4 mA, Figure 4b). While without bias (0 V), only a small built-in electric field formed at the depletion region acts as the driving force to separate the carriers, so that the photocurrent/responsivity becomes much lower (≈2 nA, Figure 5b). Thus, a marked change for UV to visible rejection ratio is obtained at zero bias (Table 1). The current exhibits good switching behaviors at zero bias under chopped light illumination without decay (Figure 5b). Note that there is an obvious current spike when switching on the light without an external potential, reflecting the large concentration of photogenerated carriers accumulated at the interface which cannot be recombined in time, leading to an unstable photocurrent.[51] This phenomenon will disappear when a 3 V bias has been applied (Figure 4c), demonstrating the fully potential-assisted charge separation. Moreover, it endows a very fast response speed with rise/fall time within 1 s (Figure S10, Supporting Information, 0.6 s/0.5 s). Compared to the values at 3 V (2.3 s/2.2 s, Figure S8, Supporting Information), the ultrafast response speed at zero bias is due to the higher energy barrier and the shorter lifetime of the photoinduced carriers.

The optical properties are determined by UV–vis diffuse reflectance spectra (DRS, Figure S11, Supporting Information), in which the pristine TiO_2 and PEDOT:PSS/TiO_2 hybrid exhibit a similar profile. The dominant peak at 365 nm in the UV range is ascribed to the large energy band gap of anatase TiO_2 (≈3.17 eV using Kubelka–Munk equation, Figure 5c). The weak absorption in the visible light region (400–800 nm) of TiO_2 is originated from the light scattering effect caused by pores/cracks in the NTs.[25] The enhanced visible light

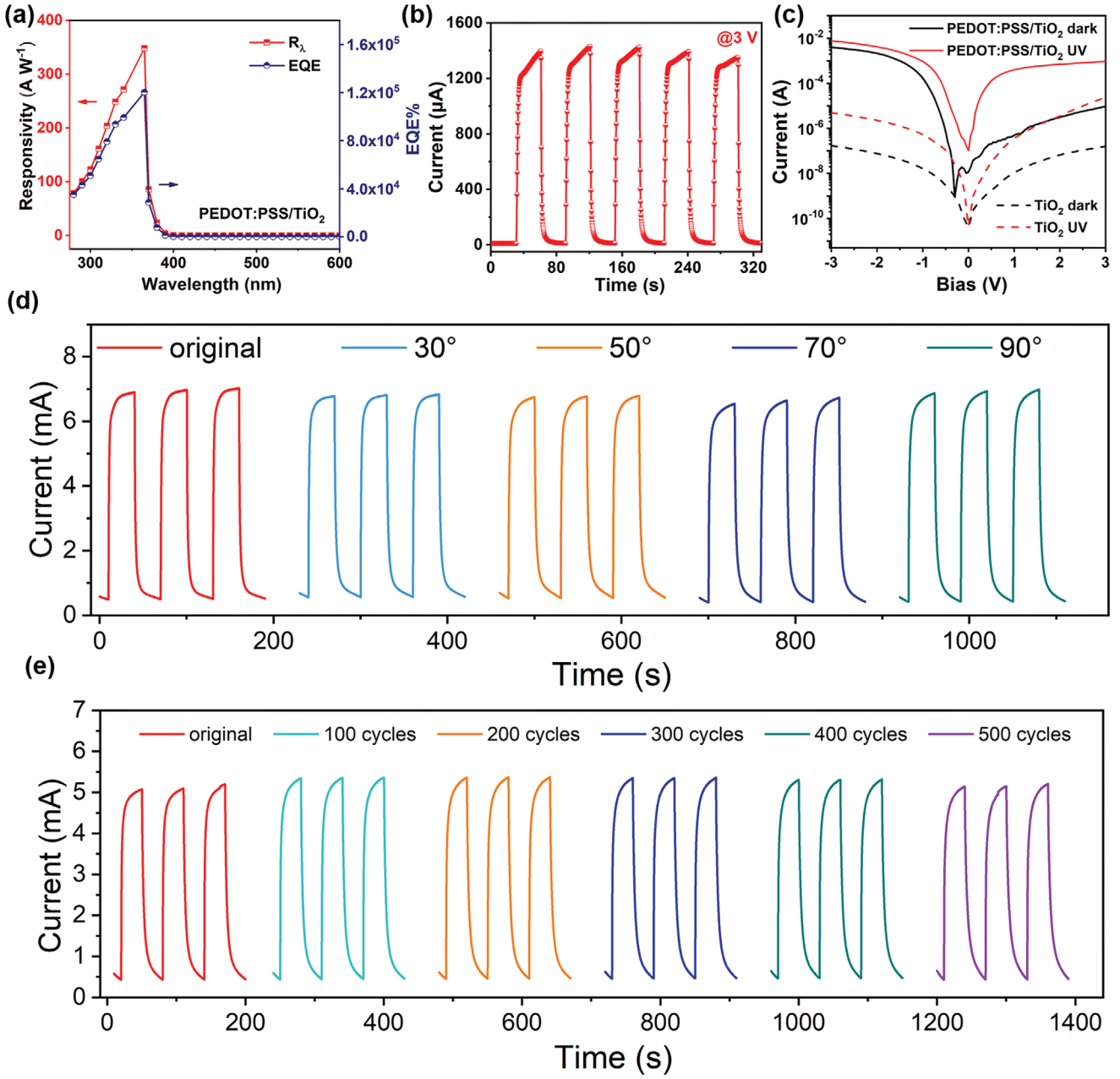

Figure 4. Photoelectric properties of PEDOT:PSS/TiO_2 FPD. a) Responsivity and quantum efficiency at 3 V. b) *I–t* curves at 3 V and c) *I–V* curves under 365 nm UV illumination. *I–t* curves at 3 V bias under 365 nm UV illumination d) at different bending angles and e) after being bent at 90° for different cycles.

Table 1. The photoelectric performance of 1D FPDs in this study.

Device	Bias [V]	Photocurrent	Rise/fall time	$R_{365\ nm}$	Rejection ratio R_{365}/R_{400}	Detectivity (365 nm)	EQE [%]
TiO_2	3	≈8 μA	16.5 s/22.6 s	1.56 A W^{-1}	14.8	3.56×10^{11}	5.56×10^{2}
H-TiO_2	3	110 μA	0.8 s/19.4 s	24.62 A W^{-1}	–	5.86×10^{11}	8.50×10^{3}
PEDOT:PSS/TiO_2	3	≈1400 μA	2.3 s/2.2 s	348.46 A W^{-1}	436	7.01×10^{12}	1.20×10^{5}
	0	1.95 nA	0.6 s/0.5 s	5.1 mA W^{-1}	2.0	2.61×10^{10}	
H-PEDOT:PSS/TiO_2	0	100 nA	0.5 s/0.2 s	161 mA W^{-1}	3.53	8.87×10^{10}	

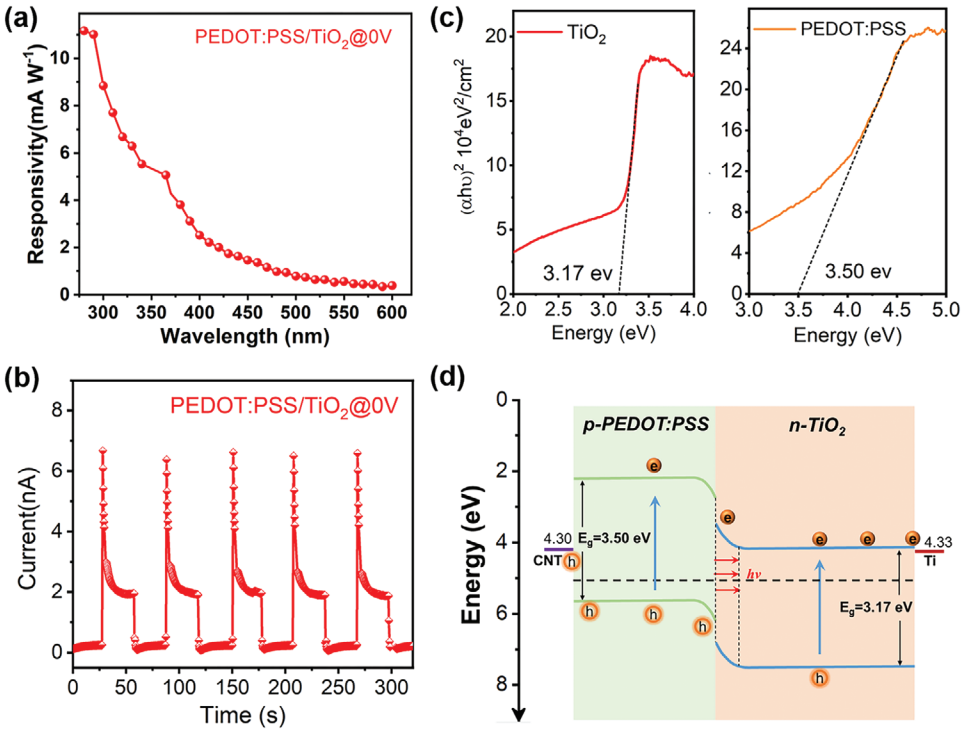

Figure 5. Photoelectric property of the PEDOT:PSS/TiO_2 FPD in the self-powered mode. a)The R_λ evolution with wavelength at zero bias. b) *I–t* curves at 0 V bias. c) The Kubelka–Munk conversion spectra of TiO_2 and PEDOT:PSS. d) Schematic diagram of the energy levels in PEDOT:PSS/TiO_2 hybrid.

absorption of PEDOT:PSS/TiO_2 and PEDOT:PSS is associated with the free charge carriers in PEDOT. While the strong absorption in the UV region for PEDOT:PSS is ascribed to the phenyl moieties in PSS component (Figure S11b, Supporting Information).[40] Its optical band gap energy is calculated to be 3.5 eV using Kubelka–Munk equation (Figure 5c). In order to further confirm the band edge positions of TiO_2 and PEDOT:PSS,[52] ultraviolet photoelectron spectroscopy (UPS) has been performed and the results are shown in Figure S12, Supporting Information. The energy levels of PEDOT:PSS/TiO_2 heterojunction and the charge transfer process upon UV illumination are schematically illustrated in Figure 5d. The device presents a type-II heterojunction with band bending at the interface, which creates a built-in electric field. Upon UV light illumination, photogenerated electrons and holes are quickly separated by the built-in electric field in the depletion layer. Specifically, the holes shift from the valence band of TiO_2 to the highest occupied molecular orbital (HOMO) of PEDOT:PSS, and then be gathered by the CNT yarn electrode (work function of 4.30 eV).[23] Meanwhile, the electrons move toward the conduction band of TiO_2, resulting in the formation of considerable photovoltage at the interface to produce a stable photocurrent.[14] Compared with traditional 2D devices, the fibrous device configuration impels the photogenerated carriers to drift along the longitudinal direction of TiO_2 NTs and arrive at the outer/inner electrodes,[49] which is beneficial to the effective and rapid separation of carriers, leading to the enhanced photoresponse.

The photoelectric performance of the constructed H-PEDOT:PSS/TiO_2 FPD is presented in **Figure 6**. The main parameters of the FPDs are listed in Table 1. The *I–V* curves under dark and 365 nm illumination (Figure 6a) indicate typical photodiode behavior and obvious self-powered property. The rectification ratio at ±3 V is calculated to be 728, almost twice higher than that of PEDOT:PSS/TiO_2 FPD, with an open-circuit voltage of ≈0.3 V. The responsivity spectrum at 3 V is presented in Figure S13, Supporting Information, which shows a maximum responsivity at 350 nm and a sharp cutoff wavelength at 400 nm, suggesting high wavelength selectivity in the solar-blind region. The *I–t* curves (Figure 6b,c) demonstrate a prominent current spike followed by a steady photocurrent of ≈100 nA with rise/fall time of 0.52 s/0.21 s at 0 V, with a stable and fast photoresponse in the self-powered mode. The responsivity reaches 161 mA W^{-1} at 0 V under 365 nm illumination (Figure 6d), outperforming most of the recently reposted fibrous PDs in literature (Table S1, Supporting Information).[24,25] By comparison, H-PEDOT:PSS/TiO_2 FPD device displays dramatically enhanced responsivity at 0 V bias: is ≈32 times higher than that of PEDOT:PSS/TiO_2 FPD at 0 V (i.e., enhancement of 3200%, Figure 6e). The D^* of the FPD obtained using Equation (3) is 8.87×10^{10} Jones (Figure 6f) under 365 nm irradiation, which is 3.3 times higher than that of the untreated FPD counterpart ($D^* = 2.61 \times 10^{10}$ Jones). Figure 6g,h shows the outstanding flexibility performance of the self-powered H-PEDOT:PSS/TiO_2 FPD under deformation state. The FPD exhibits a stable and reproducible UV response under 365 nm illumination at 0 V bias. Even after bending at 90° for 0–500 cycles, the photocurrent still holds over 90% of its initial value at the free states, suggesting its potential of working under different circumstances (like a ring or a helix).

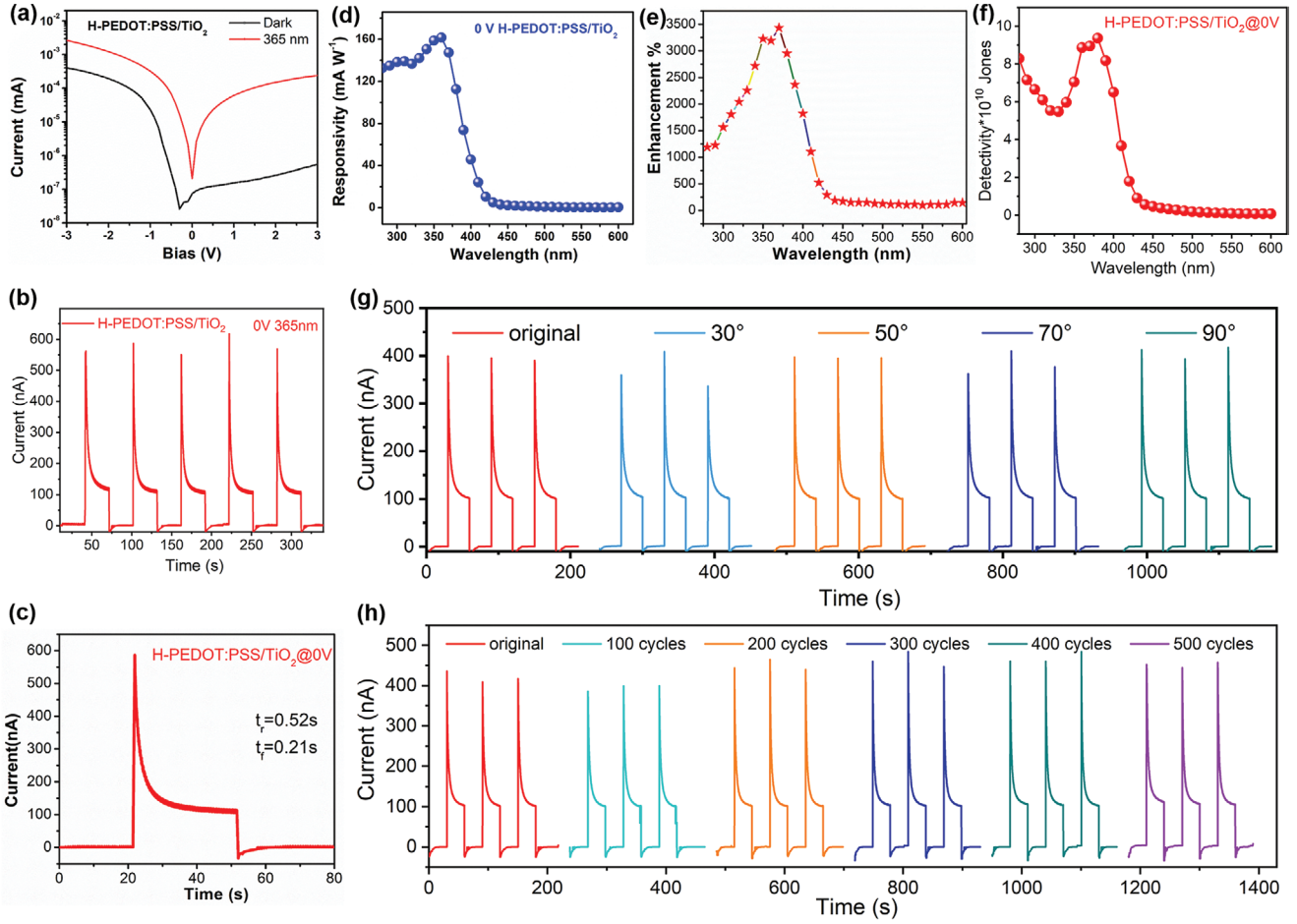

Figure 6. The optoelectronic performance of H-PEDOT:PSS/TiO_2 FPD in self-powered mode. a) *I–V* curves under dark and 365 nm UV light illumination, b) *I–t* curve, and c) enlarged *I–t* curve in one cycle, d) responsivity spectra and e) responsivity enhancement compared with PEDOT:PSS/TiO_2 FPD, f) detectivity spectra at zero bias. *I–t* curves at 0 V bias under UV illumination g) at bending angles of 0-30-50-70-90° at 0 V and h) after bending at 90° for different cycles.

The underlying mechanism that responsible for the huge responsivity enhancement of self-powered H-PEDOT:PSS/TiO_2 FPD is carefully investigated from TiO_2 and PEDOT:PSS respective aspects. For TiO_2 domain, the H-TiO_2 FPD exhibits a bit higher dark current (Figure S14, Supporting Information) and a stronger photocurrent at 3 V (110 µA) with quicker response speed (0.8 s/19.4 s, Figure S15, Supporting Information) compared to the performance of pure TiO_2 FPD (Table 1), verifying the enhanced conductivity and better photoresponse. The reason can be explained by the facilitated charge transportation and suppressed charge recombination enabled by the decreased tube wall thickness after acid treatment, which is consistent with the results in literature.[53,54] On the other hand, for PEDOT:PSS, the film resistance of PEDOT:PSS (**Figure 7**a, Figure S16, Supporting Information) reduces from 80% to 4% after concentrated acid treatment, leading to the greatly enhanced conductivity, and thus the remarkably improved photocurrent (from 1.95 to 100 nA at 0 V bias, Table 1). X-ray photoelectron spectroscopy (XPS) is also used to probe the structural change of PEDOT:PSS after H_2SO_4 treatment. Figure 7b shows the S 2p spectra, which display doublets corresponding to the $S2p_{3/2}$ and $S2p_{1/2}$, respectively. The lower binding energy peak at 162.0–166.5 eV indicates the sulfur in the thiophene ring of PEDOT while the higher binding energy peak at 167.6–173.0 eV refers to the sulfur in the sulphonic acid of PSS.[55] For H:PEDOT:PSS, the intensity of peak assigning to PEDOT is remarkably strengthened while the intensity for PSS peak is largely decreased, which is probably related to the significant reduction of insulating PSS component in the PEDOT:PSS organic film.[32] Furthermore, the S 2p binding energy of PEDOT shifts toward a lower binding energy level, owing to the replacement of polyanions PSS by HSO_4^- ions or SO_4^{2-} ions or both of them during an ion exchange process.[56] As a result, the heterojunction interface is greatly modified owing to the thinner tube wall thickness of TiO_2 and massive exposure of conducting PEDOT domain after acid treatment, and the strengthened junction effect leads to superb self-powered performance. Based on the above analysis, the working model is proposed, as illustrated in Figure 7c. When treated with highly concentrated H_2SO_4, autoprotolysis is taking place following the equation to produce two ions: $2H_2SO_4 \leftrightarrow H_3SO_4^+ + HSO_4^-$, which could stabilize the segregated states of the positively charged PEDOT and negatively charged PSS. Then, the strong π–π stacking nature of PEDOT and the rigidity of its backbone

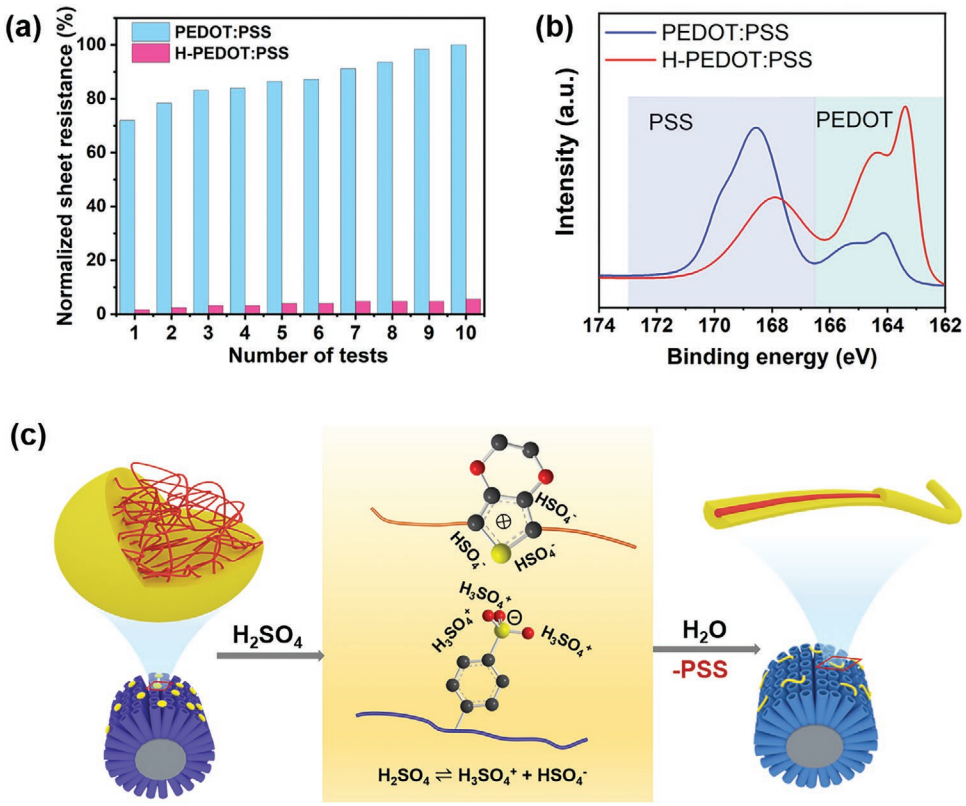

Figure 7. a) Normalized sheet resistance and b) S 2p XPS spectra of PEDOT:PSS and H-PEDOT:PSS film. c) The scheme of the removal of PSS via a concentrated sulfuric acid treatment.

induce dense PEDOT networks with significant changes in the morphological structures via the formation of nanofiber structure.[40] In this process, the H_2SO_4 and the excessive amount of uncoupled PSS are washed out by a sufficient amount of water, whereas a minimal amount of PSS is reorganized with PEDOT and acts as a counter-ion.

The UV–vis DRS of H-PEDOT:PSS (Figure S17a, Supporting Information) reveals an obvious and large light absorption improvement in the range of 280–800 nm, which is possibly attributed to the increased exposure of PEDOT core.[40] This large change is also reflected in the optical band gap energy of H-PEDOT:PSS, which is dramatically decreased to ≈2.44 eV compared to that of PEDOT:PSS (3.5 eV, Figure 5c). Based on the UPS results (Figures S12 and S17, Supporting Information), H-PEDOT:PSS endows a higher HOMO edge position (Δ+0.1 eV) in contrast to pristine PEDOT:PSS (5.9 eV) and a lower lowest unoccupied molecular orbital (LUMO) edge position (Δ–0.96 eV). The much lower LUMO position definitely facilitates the electron transfer from LUMO of H-PEDOT:PSS to the conduction band of TiO_2 and finally be collected by the inner Ti electrode (Figure S18, Supporting Information). On the other hand, the slightly increased HOMO position of H-PEDOT:PSS is conductive to the hole injection from the valence band of TiO_2 to polymer. Thus, it is more conducive to hampering the recombination of photogenerated charge carriers. To further analyze the effect of acid treatment on the p-n junction, the diode parameters such as ideality factor (n) and barrier height (ϕ_b) of PEDOT:PSS/TiO_2 and H-PEDOT:PSS/TiO_2 devices are determined (see Figure S19 and Note S1, Supporting Information). Compared to PEDOT:PSS/TiO_2 device, the n value for H-PEDOT:PSS/TiO_2 device is increased from 3.98 to 4.52. For an ideal p–n junction, the ideality factor n should be 1 at low bias and 2 at high bias based on the Sah–Noyce–Shockley model.[57] The much larger n value in our case can be attributed to the presence of surface trap states in acid-treated TiO_2 verified by the low crystallinity, which provides multiple current pathways at the p–n junction interface and thereby increasing the efficiency of charge separation.[57–59] The barrier height ϕ_b can also be calculated from the equation with a value increasing from 0.71 to 0.73 eV. This phenomenon could be ascribed to the higher HOMO position (Δ+0.10 eV) for H-PEDOT:PSS compared with PEDOT:PSS (Figures S12 and S17, Supporting Information), which broaden the space-charge region and enhance the built-in electric field.[60,61] As a result, it leads to efficient charge separation and transport and finally excellent self-powered photodetection property in H-PEDOT:PSS/TiO_2 device.

3. Conclusion

In summary, a novel inorganic–organic PEDOT:PSS/TiO_2 FPD is successfully fabricated, which shows a high responsivity, good UV-visible rejection ratio, and high EQE at 3 V under 365 nm UV illumination. It also can be worked under self-powered mode with fast response speed. Unexpectedly,

after concentrated H_2SO_4 post-treatment, the self-powered property of H-PEDOT:PSS/TiO_2 FPD device can be significantly enhanced, endowing a high responsivity of 161 mA W^{-1} and fast response speed (<1 s) due to the strongly improved conductivity. The responsivity enhancement is calculated to be approximately 3100% compared with PEDOT:PSS/TiO_2 FPD at 0 V bias under 365 nm UV light illumination. This work shows that the inorganic–organic FPDs have great potential for future wearable electronic devices.

4. Experimental Section

Synthesis of TiO_2 NTs: Ti metallic fiber (99.6%, diameter of ≈0.1 mm) was cleaned with acetone, ethanol, and deionized water, and then dried in a nitrogen stream. A conventional two-step anodization method was used to grow TiO_2 NTs in a two-electrode cell. A mixture of NH_4F (0.36 wt%, Aladdin, 98%) and deionized water (2 wt%) in the ethylene glycol (Aladdin, 98%) was served as the electrolyte. The first anodization process was conducted at 60 V for 2 h, and the obtained oxide thin-film was peeled off by ultrasonication. Then the Ti fiber underwent a second anodization process using the fresh electrolyte at 60 V for 10 min. After washing with ethanol and deionized water, the anodized Ti fiber was annealed in air at 450 °C for 2 h to yield anatase TiO_2 NTs.

Synthesis of PEDOT:PSS/TiO_2 Hybrid: The loading of PEDOT:PSS organic polymer was followed a vacuum impregnation method from our previous report.[25] The synthesized TiO_2 NTs fiber was placed in a bottle which was sealed to pump vacuum for 2 h. PEDOT:PSS (ORGACIN Dry, AGFA) dispersed in ethyl alcohol with a concentration of 5 mg mL^{-1} was injected and remained in vacuum for another 2 h. The PEDOT:PSS/TiO_2 hybrid was obtained after washing with ethanol and drying at 120 °C for 15 min for a better interface.

Synthesis of H-PEDOT:PSS/TiO_2 Hybrid and H-TiO_2 NTs: Similarly, the acid-treatment was performed under vacuum. Briefly, the PEDOT:PSS/TiO_2 hybrid fiber was transferred to the bottle and pumping vacuum for 2 h. Concentrated sulfuric acid was injected into the bottle and kept in vacuum condition for another 8 h. Then the fiber was taken out to soak in deionized water overnight to remove the extra acid and then heated at 120 °C for 15 min to give H-PEDOT:PSS/TiO_2 hybrid. Replacing PEDOT:PSS/TiO_2 hybrid fiber with TiO_2 NT fiber can yield H-TiO_2 NTs.

Synthesis of CNT yarn: The CNT yarn was obtained by a chemical vapor deposition spinning method.[49] The ethanol/acetone was used as the carbon source, ferrocene as the catalyst, and thiophene promoter in hydrogen flow at 1250 °C.

Device Fabrication and Photoelectric Measurements: To assemble FPDs, one end of the metal fiber was polished to expose the conductive Ti and used as the inner electrode. CNT yarn was tightly twisted around the photoactive materials on the metallic fiber and the extended part served as the outer electrode (Scheme S1, Supporting Information). The effective fiber length was fixed at 0.5 cm for each sample. The photoelectric performance was tested on Keithley 4200-SCS and a Xe arc lamp (70 W) with a monochromator was the light source. The light intensity was determined with a NOVA II power meter (OPHIR Photonics). All the measurements were performed at room temperature.

Characterization: The morphology was characterized using scanning electron microscopy (SEM, ZEISS GeminiSEM, Germany) and a high-resolution TEM (HRTEM, FEI, Tecnai G2 F30). XRD patterns were recorded with a PANalytical X'Pert PRO powder diffractometer using Cu Kα radiation (λ = 0.1541 nm) operating at 40 kV and 40 mA. Raman spectroscopy (Renishaw invia Raman microscope) was performed using 532 nm laser. UPS was tested with a monochromatic He I light source (21.2 eV) and was analyzed by VG Scienta R4000. The UV–vis diffuse reflectance spectra (DRS) of the samples were recorded on a UV2700 spectrophotometer (SHIMADZU). X-ray photoemission spectroscopy (XPS, Axis Ultra, Kratos) was used to test the electronic structures.

Supporting Information

Supporting Information is available from the Wiley Online Library or from the author.

Acknowledgements

This work was supported by the National Natural Science Foundation of China (51702287 and 1201101405) and the Natural Science Foundation of Zhejiang Province (LY21B030005).

Conflict of Interest

The authors declare no conflict of interest.

Data Availability Statement

Research data are not shared.

Keywords

acid treatment, fiber photodetectors, PEDOT:PSS/TiO_2 heterojunction, responsivity enhancement, self-powered photodetectors

Received: March 22, 2021
Revised: May 31, 2021
Published online: August 3, 2021

[1] T. P. Huynh, H. Haick, *Adv. Mater.* **2018**, *30*, 1802337.
[2] C. T. Lambert, J. M. Bumgarner, K. G. Tarakji, *JAMA, J. Am. Med. Assoc.* **2019**, *321*, 2367.
[3] M. Sang, S. Wang, S. Liu, M. Liu, L. Bai, W. Jiang, S. Xuan, X. Gong, *ACS Appl. Mater. Interfaces* **2019**, *11*, 47340.
[4] W. Wu, H. Haick, *Adv. Mater.* **2018**, *30*, 1705024.
[5] S. Lee, A. Nathan, *Science* **2016**, *354*, 302.
[6] H. Jinno, K. Fukuda, X. M. Xu, S. Park, Y. Suzuki, M. Koizumi, T. Yokota, I. Osaka, K. Takimiya, T. Someya, *Nat. Energy* **2017**, *2*, 780.
[7] P. C. Y. Chow, T. Someya, *Adv. Mater.* **2020**, *32*, 1902045.
[8] A. Guimarães de Oliveira, J. P. Nascimento, H. de Fátima Gorgulho, P. B. Martelli, C. A. Furtado, J. L. Figueiredo, *J. Alloys Compd.* **2016**, *654*, 514.
[9] J. Woo, H. Lee, C. Yi, J. Lee, C. Won, S. Oh, J. Jekal, C. Kwon, S. Lee, J. Song, B. Choi, K. I. Jang, T. Lee, *Adv. Funct. Mater.* **2020**, *30*, 1910026.
[10] W. Yan, A. Page, T. Nguyen-Dang, Y. Qu, F. Sordo, L. Wei, F. Sorin, *Adv. Mater.* **2019**, *31*, 1802348.
[11] L. Wei, C. Hou, E. Levy, G. Lestoquoy, A. Gumennik, A. F. Abouraddy, J. D. Joannopoulos, Y. Fink, *Adv. Mater.* **2017**, *29*, 1603033.
[12] F. R. Fan, W. Tang, Z. L. Wang, *Adv. Mater.* **2016**, *28*, 4283.
[13] S. Y. Li, Y. Zhang, W. Yang, H. Liu, X. S. Fang, *Adv. Mater.* **2020**, *32*, 1905443.
[14] Y. Zhang, S. Li, W. Yang, M. K. Joshi, X. S. Fang, *J. Phys. Chem. Lett.* **2019**, *10*, 2400.
[15] M. Hu, F. Teng, H. Chen, M. Jiang, Y. Gu, H. Lu, L. Hu, X. S. Fang, *Adv. Funct. Mater.* **2017**, *27*, 1704477.
[16] F. Teng, K. Hu, W. Ouyang, X. S. Fang, *Adv. Mater.* **2018**, *30*, 1706262.

[17] H. Wang, D. H. Kim, *Chem. Soc. Rev.* **2017**, *46*, 5204.
[18] S. Cai, X. Xu, W. Yang, J. Chen, X. S. Fang, *Adv. Mater.* **2019**, *31*, 1808138.
[19] S. F. Leung, K. T. Ho, P. K. Kung, V. K. S. Hsiao, H. N. Alshareef, Z. L. Wang, J. H. He, *Adv. Mater.* **2018**, *30*, 1704611.
[20] P. P. Yu, K. Hu, H. Y. Chen, L. X. Zheng, X. S. Fang, *Adv. Funct. Mater.* **2017**, *27*, 1703166.
[21] Z. Hou, G. Li, C. Ling, H. Wang, L. Zhu, T. Guo, T. Zhang, B. Feng, M. Cao, Q. Xue, *Adv. Electron. Mater.* **2020**, *6*, 2000501.
[22] W. Peng, X. Wang, R. Yu, Y. Dai, H. Zou, A. C. Wang, Y. He, Z. L. Wang, *Adv. Mater.* **2017**, *29*, 1606698.
[23] Y. H. Dong, Y. S. Zou, J. Z. Song, Z. F. Zhu, J. H. Li, H. B. Zeng, *Nano Energy* **2016**, *30*, 173.
[24] H. Sun, W. Tian, F. Cao, J. Xiong, L. Li, *Adv. Mater.* **2018**, *30*, 1706986.
[25] L. Zheng, X. Deng, Y. Wang, J. Chen, X. S. Fang, L. Wang, X. Shi, H. Zheng, *Adv. Funct. Mater.* **2020**, *30*, 2001604.
[26] H. Chen, P. Yu, Z. Zhang, F. Teng, L. Zheng, K. Hu, X. S. Fang, *Small* **2016**, *12*, 5809.
[27] E. A. Mojtabavi, S. Nasirian, *Appl. Surf. Sci.* **2019**, *492*, 189.
[28] V. Galstyan, E. Comini, G. Faglia, G. Sberveglieri, *Sensors* **2013**, *13*, 14813.
[29] K. Du, G. H. Liu, X. Y. Chen, K. Y. Wang, *J. Electrochem. Soc.* **2015**, *162*, E251.
[30] L. Zheng, F. Teng, X. Ye, H. Zheng, X. S. Fang, *Adv. Energy Mater.* **2020**, *10*, 1902355.
[31] S. T. Keene, T. P. A. van der Pol, D. Zakhidov, C. H. L. Weijtens, R. A. J. Janssen, A. Salleo, Y. van de Burgt, *Adv. Mater.* **2020**, *32*, 2000270.
[32] S. D. Xu, M. Hong, X. L. Shi, Y. Wang, L. Ge, Y. Bai, L. Z. Wang, M. Dargusch, J. Zou, Z. G. Chen, *Chem. Mater.* **2019**, *31*, 5238.
[33] S. Dhar, P. Chakraborty, T. Majumder, S. P. Mondal, *ACS Appl. Mater. Interfaces* **2018**, *10*, 41618.
[34] S. Dhar, T. Majumder, S. P. Mondal, *ACS Appl. Mater. Interfaces* **2016**, *8*, 31822.
[35] J. S. Yeo, J. M. Yun, D. Y. Kim, S. Park, S. S. Kim, M. H. Yoon, T. W. Kim, S. I. Na, *ACS Appl. Mater. Interfaces* **2012**, *4*, 2551.
[36] Y. Xia, K. Sun, J. Ouyang, *Adv. Mater.* **2012**, *24*, 2436.
[37] M. Vosgueritchian, D. J. Lipomi, Z. Bao, *Adv. Funct. Mater.* **2012**, *22*, 421.
[38] D. Alemu, H.-Y. Wei, K.-C. Ho, C.-W. Chu, *Energy Environ. Sci.* **2012**, *5*, 9662.
[39] L. Biessmann, N. Saxena, N. Hohn, M. A. Hossain, J. G. C. Veinot, P. Mueller-Buschbaum, *Adv. Electron. Mater.* **2019**, *5*, 1800654.
[40] N. Kim, S. Kee, S. H. Lee, B. H. Lee, Y. H. Kahng, Y.-R. Jo, B.-J. Kim, K. Lee, *Adv. Mater.* **2014**, *26*, 2268.
[41] K. I. Murai, K. Endo, T. Nakagawa, A. Yamahata, T. Moriga, *Int. J. Mod. Phys.: Conf. Ser.* **2012**, *6*, 19.
[42] L. Qiu, Y. Wang, D. Pang, F. Ouyang, C. Zhang, *Catal. Commun.* **2016**, *78*, 22.
[43] L. Zheng, S. Han, H. Liu, P. Yu, X. S. Fang, *Small* **2016**, *12*, 1527.
[44] B. Y. Ouyang, C. W. Chi, F. C. Chen, Q. F. Xi, Y. Yang, *Adv. Funct. Mater.* **2005**, *15*, 203.
[45] S. Garreau, G. Louarn, J. P. Buisson, A. G. Froyer, S. Lefrant, *Macromolecules* **1999**, *32*, 6807.
[46] M. H. Lee, L. X. Chen, N. Li, F. R. Zhu, *J. Mater. Chem. C* **2017**, *5*, 10555.
[47] S. Bontapalle, S. Varughese, *Polym. Degrad. Stab.* **2020**, *171*, 109025.
[48] T. R. B. Foong, Y. Shen, X. Hu, A. Sellinger, *Adv. Funct. Mater.* **2010**, *20*, 1390.
[49] X. Xu, J. Chen, S. Cai, Z. Long, Y. Zhang, L. Su, S. He, C. Tang, P. Liu, H. Peng, X. S. Fang, *Adv. Mater.* **2018**, *30*, 1803165.
[50] L. Zheng, P. Yu, K. Hu, F. Teng, H. Chen, X. S. Fang, *ACS Appl. Mater. Interfaces* **2016**, *8*, 33924.
[51] J. R. Manders, T. H. Lai, Y. B. An, W. K. Xu, J. Lee, D. Y. Kim, G. Bosman, F. So, *Adv. Funct. Mater.* **2014**, *24*, 7205.
[52] J. Liu, Y. Liu, N. Liu, Y. Han, X. Zhang, H. Huang, Y. Lifshitz, S. T. Lee, J. Zhong, Z. Kang, *Science* **2015**, *347*, 970.
[53] H. Li, J. Qu, Q. Cui, H. Xu, H. Luo, M. Chi, R. A. Meisner, W. Wang, S. Dai, *J. Mater. Chem.* **2011**, *21*, 9487.
[54] P. Lv, W. Fu, Y. Mu, H. Sun, T. Liu, J. Wang, J. Niu, X. Li, L. Liu, H. Yang, *J. Mater. Chem. A* **2015**, *3*, 16089.
[55] S. Mahato, J. Puigdollers, C. Voz, M. Mukhopadhyay, M. Mukherjee, S. Hazra, *Appl. Surf. Sci.* **2020**, *499*, 143967.
[56] J. Wang, K. Cai, S. Shen, *Org. Electron.* **2014**, *15*, 3087.
[57] C. Garrett, W. H. Brattain, *Phys. Rev.* **1955**, *99*, 376.
[58] J. S. Wright, R. Khanna, L. F. Voss, L. Stafford, B. P. Gila, D. P. Norton, S. J. Pearton, H.-T. Wang, S. Jang, T. Anderson, J. J. Chen, B. S. Kang, F. Ren, H. Shen, J. R. LaRoche, K. Ip, *Appl. Surf. Sci.* **2007**, *253*, 3766.
[59] B. K. Sharma, N. Khare, S. Ahmad, *Solid State Commun.*. **2009**, *149*, 771.
[60] Y. Ye, L. Dai, P. C. Wu, C. Liu, T. Sun, R. M. Ma, G. G. Qin, *Nanotechnology* **2009**, *20*, 375202.
[61] P. Lin, X. Yan, Z. Zhang, Y. Shen, Y. Zhao, Z. Bai, Y. Zhang, *ACS Appl. Mater. Interfaces* **2013**, *5*, 3671.